The Solar Wind Charge-eXchange Contribution to the Local Soft X-ray Background. Model to Data Comparison in the 0.1–1.0 keV Band

Dimitra Koutroumpa, Rosine Lallement, V. Kharchenko, A. Dalgarno

SSRv manuscript No.
(will be inserted by the editor)

The Solar Wind Charge-eXchange contribution to the Local Soft X-ray Background

Model to data comparison in the 0.1-1.0 keV band

Dimitra Koutroumpa · **Rosine Lallement** · **Vasili Kharchenko** · **Alex Dalgarno**

Received: date / Accepted: date

Abstract The major sources of the Soft X-ray Background (SXRB), besides distinct structures as supernovae and superbubbles (e.g. Loop I), are: (i) an absorbed extragalactic emission following a power law, (ii) an absorbed thermal component (~2×10^6 K) from the galactic disk and halo, (iii) an unabsorbed thermal component, supposedly at 10^6 K, attributed to the Local Bubble and (iv) the very recently identified unabsorbed Solar Wind Charge-eXchange (SWCX) emission from the heliosphere and the geocorona.

We study the SWCX heliospheric component and its contribution to observed data. In a first part, we apply a SWCX heliospheric simulation to model the oxygen lines (3/4 keV) local intensities during shadowing observations of the MBM 12 molecular cloud and a dense filament in the south galactic hemisphere with Chandra, XMM-Newton, and Suzaku telescopes. In a second part, we present a preliminary comparison of SWCX model results with ROSAT and Wisconsin surveys data in the 1/4 keV band.

We conclude that, in the 3/4 keV band, the total local intensity is entirely heliospheric, while in the 1/4 keV band, the heliospheric component seems to contribute significantly to the local SXRB intensity and has potentially a strong influence on the interpretation of the ROSAT and Wisconsin surveys data in terms of Local Bubble hot gas temperature.

Keywords SWCX · Heliosphere · SXRB · ISM · Local Bubble

D. Koutroumpa
UMR 7620, IPSL/Service dAéronomie, CNRS, Université Pierre et Marie Curie, Université Versailles-Saint-Quentin, Verrires-le-Buisson, France
Tel.: +33-1-64-47-42-94
Fax: +33-1-69-20-29-99
E-mail: dimitra.koutroumpa@aerov.jussieu.fr

R. Lallement
UMR 7620, IPSL/Service dAéronomie, Verrires-le-Buisson, France

V. Kharchenko
Harvard-Smithsonian Center for Astrophysics, Cambridge, MA, USA

A. Dalgarno
Harvard-Smithsonian Center for Astrophysics, Cambridge, MA, USA

1 Introduction

The surprising discovery of X-ray emission from comets (Lisse et al., 1996) led to establishing Charge-eXchange (CX) collisions between highly charged Solar Wind ions and solar system neutrals as a very efficient non-thermal mechanism of soft X-ray emission (Cravens, 1997). Cox (1998) suggested that X-ray emission induced in Solar Wind Charge-eXchange (SWCX) collisions with interstellar (IS) neutrals flowing across the Heliosphere would be an additional component of the diffuse soft X-ray background (SXRB).

Until that discovery, the SXRB was generally assumed to consist of an absorbed extragalactic emission following a power law, an absorbed thermal component ($\sim 2\times10^6$ K) associated with the galactic disk and halo, and an unabsorbed thermal component, supposedly at 10^6 K, attributed to the Local Bubble (McCammon and Sanders, 1990; Kuntz and Snowden, 2000, and references within). The Local Bubble (or Local Cavity) is defined as the region within ~100 pc of the solar system particularly devoid of dense (and cold) gas as suggested by absorption lines in nearby star spectra (Lallement et al., 2003).

The 1/4 keV background generally presents a negative correlation with the column density of Galactic neutral hydrogen (dominated by a Galactic plane to-pole variation) that strongly suggests an "absorption" model, in which the spatial structure of the SXRB is produced by absorption of a distant X-ray component (e.g., Bowyer et al., 1968; Marshall and Clark, 1984). However, the strong absorption predicted in such models was not confirmed by observation, neither was the large energy dependence of the absorption, so different solutions were needed.

At the time, the model most consistent with the data was the so-called displacement model (Sanders et al., 1977; Snowden et al., 1990a). In this model, the hot gas is in the foreground (in the Local Hot Bubble) with respect to the absorbing cool-gas regions, and higher X-ray intensities are produced in directions where the cavity has a greater extent (towards the LB chimneys at high galactic latitudes) and thus, a greater emission measure of the plasma in it.

Since the discovery of SWCX emission, it became clear very quickly that it should contaminate at an unknown level all soft X-ray observations and it should depend strongly on SW flux and abundance variations as confirmed by the Long Term Enhancements detected during the ROSAT all-sky survey (Snowden et al., 1995) and recent X-ray observations (Snowden et al., 2004; Smith et al., 2005; Henley and Shelton, 2007a). The debate concerned the amount of contamination, and how the SWCX emission level would interfere with the Local Bubble thermal emission, since the two are most probably the major components of the unabsorbed fraction of the SXRB. Post-CX geocoronal emission can also contribute, but only during very intense SW enhancements and for short and easily identified intervals (Cravens et al., 2001).

The two components, although due to completely different mechanisms (collisional excitation for thermal plasma emission and electron capture for CX emission), produce spectra in the same energy range ($E \leq 1.5$ keV) that are frequently confused. Cravens (2000) estimated that SWCX emission could be as much as the LB emission. Line ratios, though, are very sensitive to gas temperature (and abundance) for thermal emission. For example, a 10^6 keV plasma might be responsible for all IS diffuse emission at 0.25 keV, while at 2-4 $\times$ 10^6 K it might significantly contribute to the 3/4 keV diffuse emission as well (Raymond, 1988; McCammon and Sanders, 1990, and references therein). CX line ratios mainly depend on heavy SW ion relative abundances and collision energy (Beiersdorfer et al., 2001; Kharchenko and Dalgarno, 2001; Wargelin et al., 2008). Detailed spectral comparison of SWCX and thermal emission needs a spectral resolution that should allow to resolve char-

acteristic features as the O VII triplet at 0.57 keV and in general individual lines from the continuum. Such a comparison is beyond the scope of this paper.

In this paper we mainly focus on the intensity contribution of the SWCX emission to the observed (foreground) data in the 0.1 - 1.0 keV range. In section 2 we briefly present the basic simulation model that calculates the SWCX emission.

In section 3 we analyse the simulation results for the 3/4 keV range and in particular the oxygen lines (O VII at 0.57 keV and O VIII at 0.65 keV). We present typical stationary maps of oxygen lines in section 3.1 and in section 3.2 we present the dynamic model we developed to account for short-scale temporal variations of SWCX emission , with an application on the MBM 12 Suzaku observation of February, 2006. Finaly, we conclude section 3 with a summary of shadowing observations on which we applied our SWCX dynamic model and discuss the results in the 3/4 keV range (sect. 3.3).

I section 4 we present a preliminary analysis of SWCX simulation results in the 1/4 keV range that we compare to observation data from the Wisconsin sounding rocket and ROSAT satellite surveys.

Finally, in section 5 we close our paper with a general discussion on our results.

2 SWCX model description

In Koutroumpa et al. (2006) we have presented the basic stationary model calculating the SWCX emission in the inner heliosphere. We calculate self-consistently the neutral H and He density distributions in the inner heliosphere (up to ~100 AU), in response to solar gravity, radiation pressure and anisotropic ionization processes for the two neutral species. Ionization is mainly due to charge-exchange with SW protons for H atoms and to solar EUV photons for He atoms. We also consider the impact of CX on the solar wind ions distributions. This interaction is described in the following reaction:

$$X^{Q+} + [H, He] \rightarrow X^{*(Q-1)+} + [H^+, He^+] \quad (1)$$

The collision rate per volume unit $R_{X^{Q+}}$ ($cm^{-3}\ s^{-1}$) of X^{Q+} ions with the neutral heliospheric atoms is given by the equation:

$$R_{X^{Q+}}(r) = N_{X^{Q+}}(r)\,\upsilon_r\,(\sigma_{(H,X^{Q+})}\,n_H(r) + \sigma_{(He,X^{Q+})}\,n_{He}(r)) = R_{(X^{Q+},H)}(r) + R_{(X^{Q+},He)}(r) \quad (2)$$

where $\sigma_{(H,X^{Q+})}$ and $\sigma_{(He,X^{Q+})}$ are the hydrogen and helium CX cross-sections, $n_H(r)$ and $n_{He}(r)$ are the hydrogen and helium density distributions respectively, $\bar{\upsilon_r} = \bar{V_{SW}} - \bar{\upsilon_n} \approx \bar{V_{SW}}$ the relative velocity between SW ions and IS neutrals in the inner heliosphere, and $N_{X^{Q+}}(r)$ is the self-consistent solution to the differential equation:

$$\begin{aligned} \frac{dN_{X^{Q+}}}{dx} &= -N_{X^{Q+}}\,(\sigma_{(H,X^{Q+})}\,n_H(x) + \sigma_{(He,X^{Q+})}\,n_{He}(x)) \\ &\quad + N_{X^{(Q+1)+}}\,(\sigma_{(H,X^{(Q+1)+})}\,n_H(x) + \sigma_{(He,X^{(Q+1)+})}\,n_{He}(x)) \end{aligned} \quad (3)$$

expressing the evolution of the density distribution of ion X^{Q+} along SW streamlines due to production (from CX reactions of ion $X^{(Q+1)+}$) and loss terms.

Cross-section uncertainties are mainly due to instrumental systematic errors and most important to collision energy dependance of cross-sections. Detailed uncertainties for individual ions are not given in literature, but average uncertainties of ~30% at most are reported (Wargelin et al., 2008).

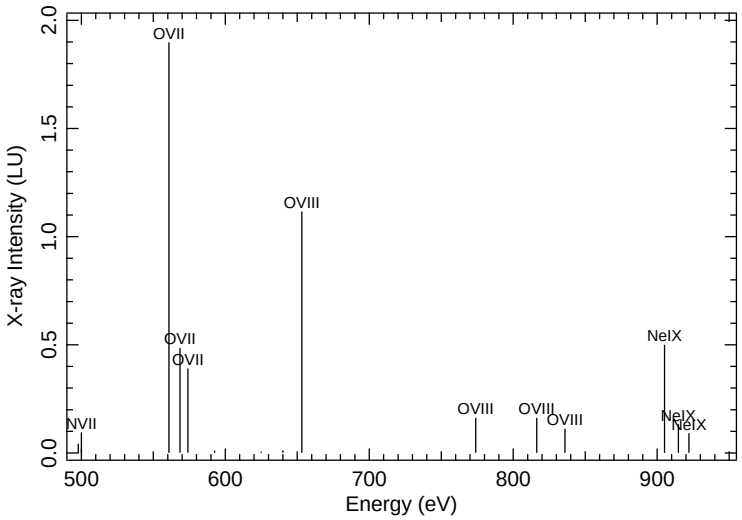

Fig. 1 SWCX model spectra in Line Units (photons cm^{-2} s^{-1} sr^{-1}) for the 3/4 keV band. The emitting ion is noted above each line.

Then, we establish emissivity grids in units of (photons cm^{-3} s^{-1}):

$$\varepsilon_i(r) = R_{(X^{Q+},H)}(r)\, Y_{(E_i,H)} + R_{(X^{Q+},He)}(r)\, Y_{(E_i,He)} \tag{4}$$

where $Y_{(E_i,M)}$ is the photon emission probability of spectral line E_i following CX with the corresponding neutral species M (H or He individually). For any line of sight (LOS) and observation date, this spectral line is given by:

$$I_{E_i}(LU) = \frac{1}{4\pi} \int_0^{\sim 100AU} \varepsilon_i(s)\, ds \tag{5}$$

which defines the average level emission of the spectral line for the particular date and LOS, as well as the solar cycle phase (minimum or maximum) corresponding at this date.

3 SWCX in the 3/4 keV Band

An example of calculated SWCX emission spectra in the 3/4 keV (0.5-1.0 keV) range is presented in figure 1. The major emission lines contributing in this energy range are:
(i) the He-like O VII multiplet, consisting of the following transitions:
- the 2^3S_1 triplet at 560.9 eV, called forbidden (O6f)
- the 2^3P_1 triplet at 568.5 eV, called intercombination line (O6i)
- the singlet state 2^1P_1 at 574 eV, usually refered to as resonance line (O6r), and
(ii) the H-like O VIII Lyman-α line at 653.1 eV.
In this list we can also add the He-like Ne IX multiplet (905.1 eV, 914.7 eV and 922.1 eV), but actual observing instruments do not always allow the detection of this line.

3.1 Stationary Model Maps

In figure 2 we present an example of calculated full-sky maps of heliospheric emission for line O VIII (0.65 keV) in ecliptic coordinates, on December, 5 (when the Earth is located downwind) of a typical solar maximum (upper panel) and solar minimum (lower panel) year. Colorscales represent O VIII line intensity given in units of 10^{-9} erg cm^{-2} sr^{-1} s^{-1}, the red colour corresponding to minimum and the blue to maximum values. We have removed from every map a data portion of 20°× 20°around the solar disk where no instrument can observe.

What we need to point out here are the striking differences between maximum and minimum solar conditions. At low latitudes, near the solar equator where slow SW dominates, X-ray emission is more intense for solar minimum than for solar maximum because the neutral atom content is higher during solar minimum. During solar minimum, photo-ionization is less efficient and H and He are less readily destroyed by photo-ionization. Since gravitational pressure exceeds radiation pressure, neutral H atoms have incoming trajectories that fill the ionization cavity.

On the other hand, at high ecliptic latitudes, LOS's are mostly affected by fast wind during solar minimum, and the X-ray emission is dominated by differences of ion relative abundances with respect to maximum cycle phase. Indeed, O^{8+} is completely absent from the fast SW and the O VIII line is expected to be much fainter at solar minimum than solar maximum, as it is seen in the maps in fig. 2.

O^{7+} has the same trend in relative abundance variations as O^{8+} between solar minimum and solar maximum. Nevertheless, instead of being completely absent in the fast wind, it is only strongly depleted ([O^{7+} / O] = 0.03) with respect to slow wind ([O^{7+} / O] = 0.2). Therefore, we expect that O VII line (0.57 keV) variations from solar maximum to solar minimum will also have the same trend as O VIII shown in the maps.

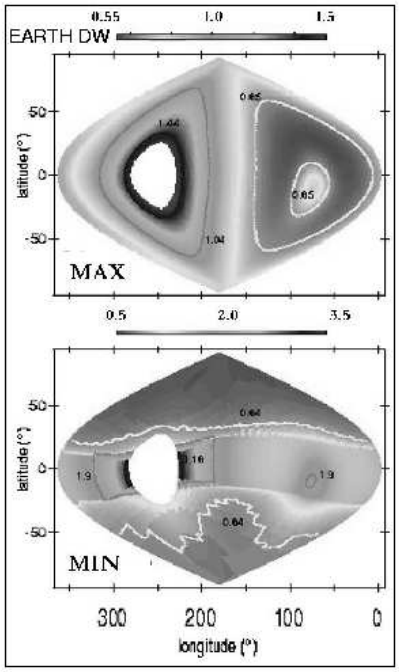

Fig. 2 Calculated full sky maps in ecliptic coordinates of the 0.65 keV O VIII line for solar maximum (upper panel) and solar minimum (lower panel) conditions. The observer is situated downwind (ecliptic longitude 75°). Colorscales are in units of 10^{-9} erg cm^{-2} s^{-1} sr^{-1}.

Two excellent examples of such differences between solar minimum and maximum conditions for the same LOS, are the MBM 12 and South Galactic Filament (SGF) shadowing observations, analysed by Smith et al. (2005, 2007) and by Henley et al. (2007); Henley and Shelton (2007b,a) respectively. These fields were thoroughly analysed for their SWCX contamination in Koutroumpa et al. (2007) and the main outline and conclusions are presented in section 3.3.

The MBM 12 LOS points toward galactic coordinates (159.2°, -34.47°), which translates to (47°, 3°) in helioecliptic coordinates, very close to the ecliptic plane and inside the limits of the equatorial slow wind zone. Therefore, during solar minimum the MBM 12 exposures (Suzaku) will yield higher SWCX contamination than solar maximum exposures (Chandra) in the 3/4 keV range.

In the case of SGF, at very high southern ecliptic latitude (353°, -73°) the effect is the opposite compared to MBM 12, because it is dominated by differences in the solar ions relative abundances. Therefore, the SWCX oxygen emission in the 3/4 keV range for the SGF field is expected to be much fainter at solar minimum (Suzaku observations) than solar maximum (XMM-Newton observations).

3.2 Dynamic Simulations

In Koutroumpa et al. (2007) we presented a dynamic variant of the basic stationary SWCX model, used to simulate the heliospheric X-ray modulation due to SW proton flux and abundance variations. For each field simulated we use real-time flux and abundance measurements from *in situ* solar wind instruments (Wind, ACE-SWEPAM) and we model SW enhancements as simplified Corotating Interaction Regions (CIR) of a step function form. The total width of the CIR is defined such that the total duration of the step function is the same as the measured enhancement in SW instruments. The step function amplitude is defined so that its total area is equal to the integral of the measured flux during the same period of time.

At each instant we define the form of the CIR (as a Parker spiral) and its propagation in the interplanetary space, taking into account solid solar rotation (27-day period), the radial propagation speed, the "ignition" time on the solar disk towards each radial direction, and the total width of the CIR. Only in the cases of CMEs, we neglect the solar rotation, since radial propagation is dominating the CME structure. Depending on the CIR's width and propagation instant, we calculate the fragment of the LOS affected by the CIR and the local emissivity ε_i'(r) modified by the SW proton flux and heavy ion abundance variations. We can then reproduce the temporal variation of the X-ray intensity levels during the periods of observation in simulated lightcurves for each of our targets. Abundance variations, can be correlated or anticorrelated with proton fluxes, so they can either emphasize or compensate for the influence of the SW proton flux enhancements.

3.2.1 The Case of the MBM 12 Suzaku Observation of February 2006

The observation of MBM 12 with Suzaku on February 3-8, 2006 was performed in two consecutive exposures, ON-CLOUD (3-6/02/2006, for a total of 231 ks) and immediately after that, OFF-CLOUD (6-8/02/2006, for a total of 168 ks) (Smith et al., 2007). A detailed description of the simulation we performed on this field is given in Koutroumpa et al. (2007).

As we already explained, the MBM 12 LOS is located at (47°, 3°) of helioecliptic coordinates. In the February Suzaku observation this geometry is pointing directly toward the He cone, which is only ∼2 AU away from the observer, where the emissivity on the LOS is maximum. The observation geometry was presented in figure 1 of Koutroumpa et al. (2007). The cone, with a denser distribution of helium atoms, is acting as an amplifier to any SW flux variation.

The MBM 12 Suzaku observation was influenced by a short SW perturbation recorded at the end of the ON-CLOUD pointing. We model this enhancement as a step function in particle flux of 5.2×10^8 cm^{-2} s^{-1} propagating at a low speed (V_{SW} = 350 km s^{-1}) for 0.75

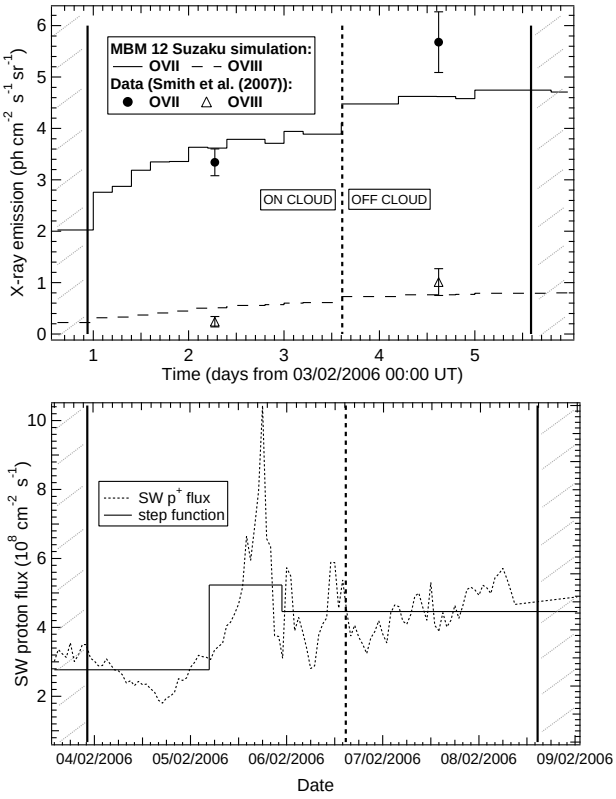

Fig. 3 *Top*: O VII and O VIII line simulated lightcurves (in LU) for the MBM12 ON and OFF observations with Suzaku during the period 03-08/02/2006. Plain line stands for the O VII emission and dashed line stands for the O VIII emission. Dots represent the measured ON and OFF O VII line flux, and triangles represent the measured ON and OFF O VIII line flux (Smith et al., 2007).
Bottom: Solar wind proton flux (dotted line) in units of 10^8 cm^{-2} s^{-1} for the same period. The step function simulating the SW enhancement is presented by the plain black line. In both panels, the vertical plain lines represent the start and end of the observation period, while the dashed vertical line is the separation between the ON and OFF exposures.

d. The SW proton flux remained at a high, but stable, level equal to 4.42×10^8 cm^{-2} s^{-1} after the spike. In the lower panel of figure 3 we present the measured SW flux curve with the dotted line and the modeled step function with the plain line.

The resulting simulated lightcurves for O VII and O VIII are shown in the upper panel of figure 3 in plain and dashed lines respectively. The plain vertical lines mark the limits of the total observing period and the dashed vertical line shows the limit between the ON and OFF cloud exposures. The dynamic model, taking into account SW measurements, is predicting a smooth but gradual rise of the oxygen line intensities in the ON and OFF exposures. The O VII and O VIII line fluxes averaged for the ON-CLOUD exposure yield 3.56 LU and 0.5 LU respectively, while averages on the OFF-CLOUD exposure yield 4.62 LU and 0.77 LU for O VII and O VIII respectively. The equivalent averaged Suzaku data for O VII and O VIII are shown in the figure with plain dots and hollow triangles respectively.

The model-data comparison for the ON-cloud exposure shows that LB emission is negligible, since the SWCX model accounts for all of the observed intensity. The X-ray flux increase (~30% and ~55% for O VII and O VIII respectively) in the OFF-CLOUD exposure would change the data interpretation in terms of hot halo gas temperature, since Smith et al. (2007) assumed a constant foreground emission.

Table 1 Comparison of shadowing observation foreground data to SWCX model for O VII and O VIII line intensities. [a] Observation date and observing instrument: C for Chandra, X for XMM-Newton and S for Suzaku. [b] MBM 12 Suzaku-off exposure is included in the analysis, as foreground emission was not constant (see §3.2.1 for details). [c] Revised values for SGF foreground line intensities, from Henley and Shelton (2007a).

		O VII (LU)			O VIII (LU)		
Target	Observation [a]	Data	Data [c]	SWCX	Data	Data [c]	SWCX
MBM 12	Aug. '00, C	1.79 ± 0.55		1.49	2.34 ± 0.36		2.13
MBM 12	Feb. '06, S-on	3.34 ± 0.26		3.56	0.24 ± 0.10		0.50
MBM 12	Feb. '06, S-off [b]	5.68 ± 0.59		4.62	1.01 ± 0.26		0.77
SGF	May, '02, X	3.40	$6.2^{+2.8}_{-2.9}$	3.16	1.00	...	1.02
SGF	Mar. '06, S	0.13	$1.1^{+1.1}_{-1.4}$	0.34	N.C.	1.0±1.1	0.02

3.3 Summary of Shadowing Observations

In Table 1 we resume the MBM 12 and South Galactic Filament shadowing observations analysed in detail in Koutroumpa et al. (2007). All four observations were simulated with the SWCX model with SW conditions as close as possible to measurements in solar instruments, to account for the SWCX contamination of the oxygen line emission in each field.

Besides the basic differences due to solar maximum or solar minimum conditions during the observing period for each field, that we reported in section 3.1, three of the four observations (MBM 12 Chandra, Suzaku and SGF XMM observations respectively) were found to be highly contaminated by short-term SWCX emission variations. In particular, in our simulations we confirmed the contamination of the MBM 12 Chandra observation by a strong CME as suggested by Smith et al. (2005). We suggested that the SGF XMM observation was also highly contaminated, most probably by a CME, which was confirmed by Henley and Shelton (2007a) when they re-analysed and compared their Suzaku and XMM data.

The observation data represent unabsorbed (attributed to the LB) O VII and O VIII line intensities as derived from the authors (Smith et al., 2005, 2007; Henley et al., 2007; Henley and Shelton, 2007b,a). In particular, for the SGF field we give two sets of data: from the initial analysis published by Henley et al. (2007) and Henley and Shelton (2007b) (values we used in Koutroumpa et al., 2007) and the revised values published by Henley and Shelton (2007a).

The shadows block more or less efficiently the Galactic Halo oxygen emission, and in their analysis the authors derive the unabsorbed foreground emission of the oxygen lines, that we use to compare to the SWCX heliospheric emission. The only exception is in the Suzaku/MBM 12 observation (Smith et al., 2007) where the O VII and O VIII halo emission is added to the foreground emission for the OFF-CLOUD exposure. Contrary to the constant foreground assumption in the Smith et al. (2007) analysis, we demonstrated that there is a ∼30% and ∼55% increase in the OFF-CLOUD simulated SWCX O VII and O VII line intensities respectively, due to the brief SW enhancement at the end of the ON-CLOUD exposure (see §3.2.1). This increase was erroneously attributed to the Galactic Halo emission, which should be revised, and thus we include these values in the analysis as well.

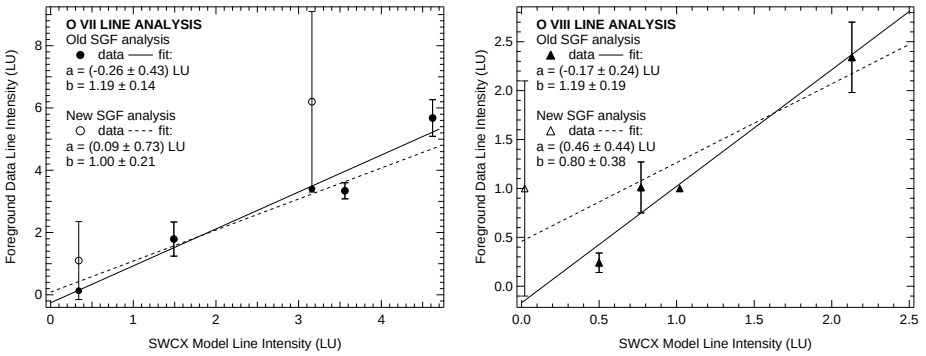

Fig. 4 Linear fits of oxygen line intensities. Foreground emission data from shadowing observations in litterature (MBM 12: Smith et al., 2005, 2007) and (SGF: Henley et al., 2007; Henley and Shelton, 2007b) versus SWCX model results for the O VII (left panel) and O VIII (right panel) line intensities. All linear fits are calculated with no error-bar weighting except for the O VII New SGF analysis fit (left panel, dashed line). See §3.3 for more details.

In figure 4 we linearly fit the data over the SWCX model results for the O VII (left panel) and O VIII (right panel) lines for the initial (plain lines) and revised (dashed lines) data sets. We did not use data errorbars as standard deviation to weight the fit, because not all data errorbars were communicated (Henley et al., 2007; Henley and Shelton, 2007b). The only exception is the O VII line fit, since Henley and Shelton (2007a) provided errorbars for both XMM and Suzaku O VII detections. The old and new fit coefficients (y(LU) = (a + bx)(LU)) for the O VII and O VIII lines are also noted on the figure.

The first linear fits (in plain lines in fig.4) we performed (Koutroumpa et al., 2007) had a slope of 1.19 (±0.14; 0.19 at 1σ for O VII and O VIII resp.) meaning that the SWCX model reproduced very well the local foreground emission measured in shadows. Moreover, the fit also gave an estimate of the residual foreground emission to be attributed to the LB. The foreground was found to be (-0.26 ± 0.43 at 1σ) LU for O VII and (-0.17 ± 0.24 at 1σ) LU for O VIII which means that with a high probability the LB O VII and O VIII emission is negligible compared to the heliospheric emission.

The new fits (in dashed lines, fig.4), where we substituted the SGF observed foreground data with the revised values of Henley and Shelton (2007a) give slightly different results, although the correlation to the simulated values remains very satisfying (the correlation is even improved for the O VII line intensities) and the residual LB emission is still consistent to zero.

4 SWCX in the 1/4 keV Band

In this section we present a preliminary study of the SWCX background in the 1/4 keV (0.1-0.3 keV) band that we compare with the ROSAT and Wisconsin surveys data. In section 4.1 we describe briefly the SWCX simulation and in section 4.2 we compare the model results with the survey data sets.

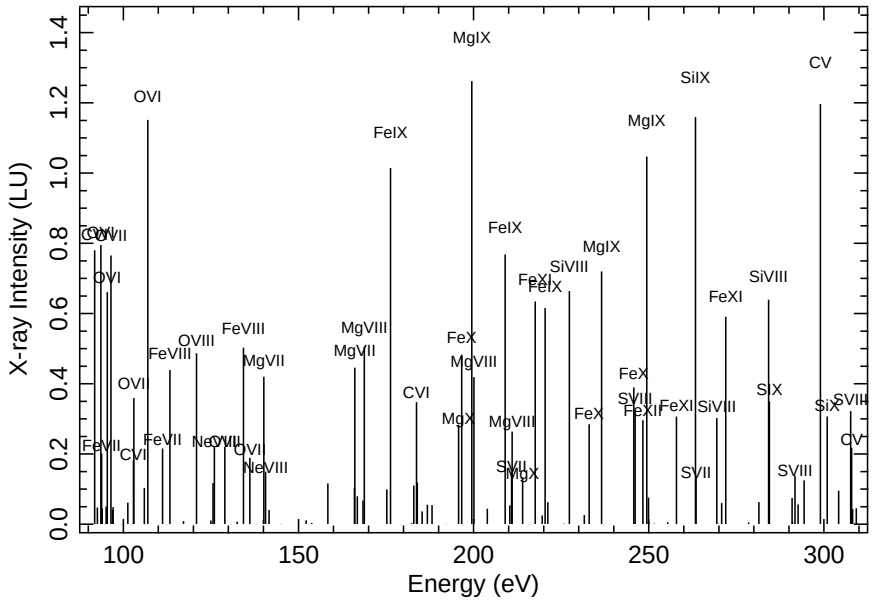

Fig. 5 Calculated SWCX spectra in Line Units for the 1/4 keV band. Emitting ions are marked above the most intense lines.

4.1 Simulations

For the study on the 1/4 keV band, we updated our atomic database to include Fe, Si, S, Mg ions that emit intense lines in the 0.1-0.3 keV range. Individual radiative transition probabilities for these ions were calculated assuming that the ions are hydrogenic. Moreover, photon yields were calculated using a unique neutral species, which means that no distinction between H and He was made. The hydrogenic ion assumption and unique neutral species choice are only approximations, but the results give a good estimate of the order of magnitude of the X-ray intensity for this energy range. An example of calculated spectra in the 0.1-0.3 keV range is presented in figure 5, with the emitting ion identifying the most intense lines.

We have calculated spectra for two LOS, upwind (UW) and downwind (DW), for an observer assumed to be at 1 AU and in a crosswind position with respect to the LOS. This observing geometry was chosen to match the ROSAT satellite observing constraints. In the 1/4 keV (0.1- 0.3 keV) range the model yields a total of 28.35 LU for the UW LOS and a total of 20.27 LU for the DW LOS. The intensity is probably underestimated because of the SW ion propagation in the heliosheath up to the heliopause, and in the heliotail up to ~3 000 AU, where all ions are used up. The outer heliospheric region is neglected (for the moment) in our model, but preliminary estimates yield a maximum additional ~20% contribution in the DW direction. In general, because of parallax effects as well, we can assume that within a 50% error bar, these values give an good estimate of average values of the heliospheric SWCX emission in the 1/4 keV range.

	SWCX model		Data range
Band	UW	DW	
B (cts s^{-1})	11.99	8.04	[20 - 100]
C (cts s^{-1})	73.32	56.24	[50 - 250]
R1 (RU [a])	141.14	104.38	
R2 (RU)	192.07	147.27	
R12 (RU)	333.21	251.65	[250 - 820]

Table 2 Summary of main band fluxes for the SWCX model in the upwind (UW) and downwind (DW) directions and measured data. For ROSAT data only the unabsorbed fraction I_o is given. [a] RU = 10^{-6} cts s^{-1} $arcmin^{-1}$.

4.2 Model-Data Comparison

The sounding rocket survey of the University of Wisconsin and the ROSAT satellite survey have dominated the diffuse SXRB observations from 1972 to 1991. The Wisconsin survey allowed a full-sky mapping of the IS SXRB with a spatial resolution of ∼7° (McCammon et al., 1983). The ROSAT survey improved the spatial resolution to ∼12' (Snowden et al., 1997). However, the instruments did not have any spectral resolution so they provided only total fluxes for each band.

In order to compare the modeled SWCX emission level to the measured SXRB intensities at 1/4 keV, we convolve the calculated spectra for the UW and DW LOS with each band response in this energy range of the instruments. The bands concerning our study are B (0.13 - 0.188 keV), C (0.16 - 0.284 keV) for the Wisconsin survey and R1 (0.08 - 0.284 keV), R2 (0.14 - 0.284 keV) for the ROSAT survey. The corresponding band responses are presented in figures: 1(a) of McCammon et al. (1983) for Wisconsin and 1 of Snowden et al. (2000) for ROSAT. In table 2 we summarize the total band fluxes derived from the SWCX spectra convolution with the band responses, and the measured data range for each band (evaluated from figures 6 and 7).

4.2.1 Wisconsin Sounding Rocket Survey

The SXRB survey of the University of Wisconsin was performed with a series of 10 sounding rocket flights between 1972 and 1979. The only spectral information in the 1/4 keV range is extracted by the boron (B) and carbon (C) filters incorporated into the detector windows that separate the two bands B and C presented in McCammon et al. (1983), figure 1(a).

Detailed maps derived from the complete survey were presented in McCammon et al. (1983). The maps present a clear negative correlation with the column density of galactic neutral hydrogen N_{HI}. The X-ray intensity is lowest toward the galactic plane and highest at high galactic latitudes. Snowden et al. (1990b) investigated the band intensity ratio B/C (low to high energies) and found a variation between 0.25 to 0.46 in a dipole-like spatial correlation, aligned with a roughly galactic center-anticenter direction, that they attributed to an anisotropy of the Local Hot Bubble temperature ranging between $10^{6.2}$ and $10^{5.9}$ K respectively.

From Snowden et al. (1990b) we extracted a scatter plot (fig.6) comparing the B and C band measurements in the Wisconsin survey. The data range is summarized in table 2 and gives ∼[20-100] cts s^{-1} for the B band and ∼[50-250] cts s^{-1} for the C band. We superposed, in this figure, the two points (wide circles) corresponding to our simulated spectra convolved with the B and C band responses (see table 2). Error bars are given only for information at

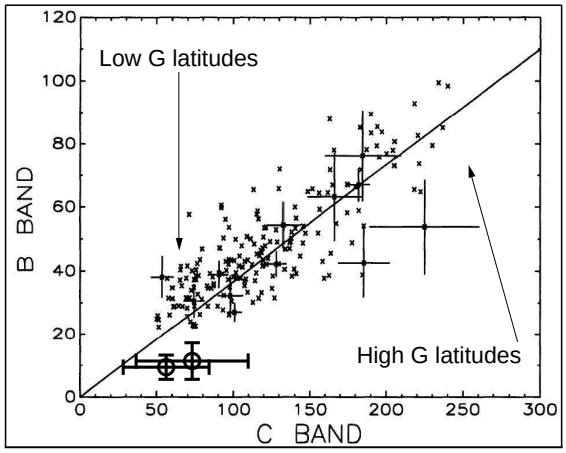

Fig. 6 Scatter plot of the total intensity calculated in the SWCX model (large circles) compared to total measured (crosses) values in B and C bands in the Wisconsin survey. The model reproduces the observed C band fluxes in the galactic plane, but not the B band fluxes. Figure extracted and adapted for our study from Snowden et al. (1990b).

50% of the SWCX band flux, in order to give an estimate of the heliospheric flux range in these bands.

The SWCX model in the C band predicts fluxes well within the observed values in the galactic plane (lower limits), but simulated B band flux is about two times lower than the lower observed limits. The band ratio B/C for the SWCX flux is accordingly inconsistent with measured values, and fairly constant from UW to DW directions, with a mean value of B/C ~ 0.15.

4.2.2 The ROSAT Survey

The ROSAT all-sky survey was performed in a scan mode with imaging telescopes in the soft X-ray band of 0.1 - 2 keV, during the first year of the mission. The observing geometry constraints imposed to scan the sky in a big circle, during one orbit, perpendicular to the spin axis that coincided with the Sun-Earth direction. Therefore a complete scan of the sky was performed in a six-month period.

The ROSAT all-sky maps in the 1/4 keV range (Snowden et al., 1995, 1997) confirmed the Wisconsin results and the negative correlation with the H I column density. The improved spatial resolution of ROSAT, with respect to previous surveys, allowed a better use of shadows as tools to separate the foreground from distant components of the SXRB. An extensive catalog of shadows in the 1/4 keV band, with fitted foreground and distant emission values was presented in Snowden et al. (2000).

In figure 7 we present a scatter plot of foreground intensity I_o measured in band R12, which is the sum of intensities in bands R1 and R2. Units are in 10^{-6} cts s^{-1} $arcmin^{-1}$, better known as ROSAT Units (RU).The figure was extracted from Snowden et al. (2000) and the authors compare the data set analysed with two different methods. The exact comparison of the two methods is beyond the scope of this paper, since what we need is just the data intensity range (250-820 RU). In the figure y = x, thus the fitted slope is one. Simulated

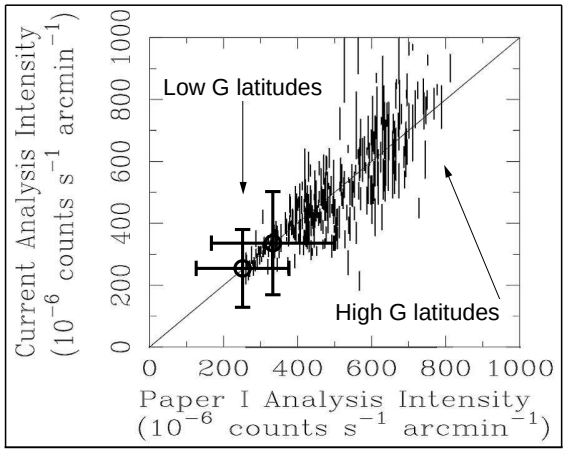

Fig. 7 Same as fig. 6 but for the unabsorbed (I_o) emission of ROSAT shadowing observations in band R12 (R1 + R2). The model reproduces most of the R12 band flux in the galactic plane. Figure extracted and adapted for our study from Snowden et al. (2000).

spectra convolved with R1 and R2 band responses and summed for the total result in R12 band yield 333.21 and 251.65 RU for the UW and DW direction respectively. These values, represented by the wide circles in fig. 7 with error bars at 50% (to give the SWCX flux range), are within the lower limits of observational data, that correspond to the low galactic latitude regions.

In the same paper (Snowden et al., 2000) confirm the dipole-like spatial correlation of the R2/R1 (high to low energies) flux ratio, although the variation is less pronounced than the one derived from the Wisconsin analysis, 1.25 to 1.04 from UW to DW. Our model results yield a constant R2/R1 ratio at an average value of 1.38.

5 Discussion

We have presented simulation results on the SWCX soft X-ray emission in the heliosphere in the 0.1-1.0 keV energy range, that we compared to data from past and present observing instruments. We separated our analysis into two energy ranges: the 3/4 keV, dominated by the oxygen (O VII and O VIII) lines and the 1/4 keV, where heavier ion lines as Mg, Si, S and Fe dominate the SWCX spectra. This analysis yields estimates of the SWCX heliospheric component within the diffuse Soft X-ray Background and confirms the large contamination of X-ray data by the heliospheric emission that needs to be taken into account in future determinations of the LB temperature and pressure.

The simulation results on shadowing clouds observed with Chandra, XMM-Newton and Suzaku suggest that the local 3/4 keV emission detected in front of shadows is entirely explained by the heliospheric SWCX emission (see table 1 and figure 4) and no emission from the LB is needed at these energies. Thus, combining our results in the 3/4 keV range and previous results published on the 3/4 and 1/4 keV ROSAT band ratios, the strict upper limit of the LB temperature is 10^6 K. Indeed, if the LB plasma is in collisional equilibrium

at 10^6 K, then it mainly emits in the 1/4 keV range, and only very little emission is produced in the oxygen lines at 3/4 keV.

But, then, how does SWCX affect the data interpretation in the 1/4 keV range? We have compared SWCX simulation results with data from the ROSAT and Wisconsin surveys. Both sets of measured data were originally interpreted in terms of hot gas emission in the LB at a temperature of $\sim 10^6$ K. Variations in the observed X-ray intensity were attributed to variations in the extent of the emission volume and therefore the emission measure of the plasma.

SWCX emission flux calculated for the R12 and C bands (which practically cover the same energy range) yielded average values that explain most of the observed emission in the galactic plane, previously attributed to the restricted regions of the LB. Indeed, according to Snowden et al. (1998), in the galactic center and anticenter directions (roughly UW and DW respectively), the LHB is found to have an extent of $R_{LHB} \sim 50$ pc (see upper left panel of figure 10 in Snowden et al., 1998), which corresponds to an unabsorbed 1/4 keV emission of $I_o = R_{LHB} / 0.155 \approx 322$ RU measured in the R12 band, while our model predicts ~[250-333] RU.

On the other hand, the SXRB intensity is typically brighter at higher Galactic latitudes, and SWCX cannot account for all the emission. This may be explained by the fact that at high latitudes the LOS's point through the chimneys allowing for non-absorbed halo emission to reach the observer. Moreover in the B band, which is the least overlapping in energy range with respect to the other 1/4 keV bands, the SWCX simulations predict about half of the observed lower limits. Besides, the SWCX model fails to reproduce the observed R2/R1 ratio by 10-33% and the B/C ratio by 40-67% .

The answer, then, to the local unabsorbed SXRB puzzle might lie in the proper mix of SWCX emission and warm (rather than hot) LB that will fill-in the gap in the B band and reproduce the observed band ratios (Koutroumpa et al., in preparation).

Acknowledgements DK and RL aknowledge The Institute for Theoretical Atomic, Molecular and Optical Physics (ITAMP) for travel and living expenses support during a visit to ITAMP facilities. The authors would like to thank Dan McCammon for providing accurate values of the effective area functions of the Wisconsin and ROSAT bands. We are also thankful to Steve Snowden for useful (and lively) discussions. Finally, we are really greatful to our referee Jeffrey Linsky for the thorough report and constructive remarks, as well as for the organisation, along with the organising comittee of the ISSI Local Bubble Workshop, of this most interesting meeting.

References

P. Beiersdorfer, C. M. Lisse, R. E. Olson, G. V. Brown, H. Chen, Astrophys. J. Letters **549**, L147–L150 (2001)

C. S. Bowyer, G. B. Field, J. F. Mack, Nature **217**, 32–+ (1968)

D. P. Cox, In *IAU Colloq. 166: The Local Bubble and Beyond*, edited by D. Breitschwerdt, M. J. Freyberg, J. Truemper, vol. 506 of *Lecture Notes in Physics, Berlin Springer Verlag*, pages 121–131 (1998)

T. E. Cravens, Geophys. Res. Lett. **24**, 105–108 (1997)

T. E. Cravens, Astrophys. J. Letters **532**, L153–L156 (2000)

T. E. Cravens, I. P. Robertson, S. L. Snowden, J. Geophys. Res. **106**, 24,883–24,892 (2001)

D. B. Henley, R. L. Shelton, ArXiv e-prints **712** (2007a)

D. B. Henley, R. L. Shelton, ArXiv Astrophysics e-prints (2007b)

D. B. Henley, R. L. Shelton, K. D. Kuntz, Astrophys. J. **661**, 304–319 (2007)

V. Kharchenko, A. Dalgarno, Astrophys. J. Letters **554**, L99–L102 (2001)

D. Koutroumpa, F. Acero, R. Lallement, J. Ballet, V. Kharchenko, Astron. Astrophys. **475**, 901–914 (2007)

D. Koutroumpa, R. Lallement, V. Kharchenko, A. Dalgarno, R. Pepino, V. Izmodenov, E. Quémerais, Astron. Astrophys. **460**, 289–300 (2006)

K. D. Kuntz, S. L. Snowden, Astrophys. J. **543**, 195–215 (2000)
R. Lallement, B. Y. Welsh, J. L. Vergely, F. Crifo, D. Sfeir, Astron. Astrophys. **411**, 447–464 (2003)
C. M. Lisse, K. Dennerl, J. Englhauser, M. Harden, F. E. Marshall, M. J. Mumma, R. Petre, J. P. Pye, M. J. Ricketts, J. Schmitt, J. Trumper, R. G. West, Science **274**, 205–209 (1996)
F. J. Marshall, G. W. Clark, Astrophys. J. **287**, 633–652 (1984)
D. McCammon, D. N. Burrows, W. T. Sanders, W. L. Kraushaar, Astrophys. J. **269**, 107–135 (1983)
D. McCammon, W. T. Sanders, Ann. Rev. Astron. Astrophys. **28**, 657–688 (1990)
J. C. Raymond, In *NATO ASIC Proc. 249: Hot Thin Plasmas in Astrophysics*, edited by R. Pallavicini, pages 3–+ (1988)
W. T. Sanders, W. L. Kraushaar, J. A. Nousek, P. M. Fried, Astrophys. J. Letters **217**, L87–L91 (1977)
R. K. Smith, M. W. Bautz, R. J. Edgar, R. Fujimoto, K. Hamaguchi, J. P. Hughes, M. Ishida, R. Kelley, C. A. Kilbourne, K. D. Kuntz, D. McCammon, E. Miller, K. Mitsuda, K. Mukai, P. P. Plucinsky, F. S. Porter, S. L. Snowden, Y. Takei, Y. Terada, Y. Tsuboi, N. Y. Yamasaki, Publ. Astron. Soc. Japan **59**, 141–150 (2007)
R. K. Smith, R. J. Edgar, P. P. Plucinsky, B. J. Wargelin, P. E. Freeman, B. A. Biller, Astrophys. J. **623**, 225–234 (2005)
S. L. Snowden, M. R. Collier, K. D. Kuntz, Astrophys. J. **610**, 1182–1190 (2004)
S. L. Snowden, D. P. Cox, D. McCammon, W. T. Sanders, Astrophys. J. **354**, 211–219 (1990a)
S. L. Snowden, R. Egger, D. P. Finkbeiner, M. J. Freyberg, P. P. Plucinsky, Astrophys. J. **493**, 715–+ (1998)
S. L. Snowden, R. Egger, M. J. Freyberg, D. McCammon, P. P. Plucinsky, W. T. Sanders, J. H. M. M. Schmitt, J. Truemper, W. Voges, Astrophys. J. **485**, 125–+ (1997)
S. L. Snowden, M. J. Freyberg, K. D. Kuntz, W. T. Sanders, Astrophys. J. Supp. **128**, 171–212 (2000)
S. L. Snowden, M. J. Freyberg, P. P. Plucinsky, J. H. M. M. Schmitt, J. Truemper, W. Voges, R. J. Edgar, D. McCammon, W. T. Sanders, Astrophys. J. **454**, 643–+ (1995)
S. L. Snowden, J. H. M. M. Schmitt, B. C. Edwards, Astrophys. J. **364**, 118–122 (1990b)
B. J. Wargelin, P. Beiersdorfer, G. V. Brown, Canadian Journal of Physics **86**, 151–169 (2008)